Optimal extraction of ultrasonic scattering features in coarse grained materials

Eduardo Lopez Villaverde, Anthony J. Croxford, Alexander Velichko

***Abstract*—Ultrasonic array imaging is used in non-destructive testing for detection and characterisation of defects. The scattering behaviour of any feature can be described by a matrix of scattering coefficients, called the scattering matrix. This information is used for characterisation, and contrary to image-based analysis, the scattering matrix allows characterisation of defects at the subwavelength scale. However, the defect scattering coefficients are in practice contaminated by other nearby scatterers or significant structural noise. In this context, an optimal procedure to extract scattering features from a selected region of interest in a beamformed image is here investigated. This work proposes two main strategies to isolate a target scatterer in order to recover exclusively the time responses of the desired scatterer. In this paper such strategies are implemented in delay-and-sum and frequency-wavenumber forms, and optimised to maximise the extraction rate. An experimental case in a polycrystalline material shows that the suggested procedures provide a rich frequency spectrum of the scattering matrix and are readily suited to minimise the effects of surrounding scattering noise. In doing so, the ability to deploy imaging methods that rely on the scattering matrix is enabled.**

***Index Terms*—Ultrasonic imaging, scattering matrix, defect characterization, grain noise.**

I. Introduction

Ultrasonic phased arrays are largely employed in non-destructive testing (NDT) for detection and characterisation of critical defects. Their location, size and orientation are key parameters to establish the risk of failure of structural components. Considerable progress has been achieved in ultrasonic array imaging providing reliable solutions for different sectors such as nuclear, aerospace, and oil and gas. Over the last decades, advanced solutions have typically been based on the post-processing of the full matrix of transmit-receive signals [1], involving application of various imaging techniques [2], [3], [4], [5] and scattering matrix analysis [6], [7] for defect characterisation.

Conventional imaging methods convert the array data into an image, which facilitates the interpretation of the data for characterisation purposes. For example, the full extent of cracks can be imaged by focusing the specular reflections of different wave mode combinations, known in the NDT community as multi-mode imaging [8], or multi-view. This technique has been studied by different research groups in order to minimise artefacts in realistic configurations [9], [10], and to estimate the length and orientation of cracks [11], [12]. However, prior knowledge of the position and shape of the defect is sometimes needed to choose the appropriate mode combination, especially in presence of complex interfaces. If the defect is smaller than the wavelength, super resolution techniques [13], [14] can be employed, but their performance is very unstable in presence of noise.

A more suitable alternative for the subwavelength scale in noisy environments is the study of defect scattering patterns. The scattering information is commonly represented by a matrix containing the far-field complex scattering coefficients for every combination of incident and scattered directions after interaction with a single scatterer. Such a scattering matrix is well suited to characterise features through the patterns of the response and can potentially enhance the sensitivity for detection purposes. However, when other scatterers are located close to the target, the measured scattering descriptor is contaminated due to the overlapping of individual responses of different scatterers. This is the case in granular structures, where grains act as randomly distributed scatterers adding a coherent structural noise to the defect signal. In addition, if used for detection purposes, the scattering matrix must be calculated at many points in an image so speed and efficiency of scattering matrix extraction is key.

In this context, there exist two methods to extract the scattering matrix from collected array data. The first is known as the subarray approach [6] where focused subapertures are synthetically created in order to increase the spatial selectivity of the array data. The limitation of this method is that it provides smoothed amplitude scattering coefficients due to the use of large subapertures. The second method is based on a reversible imaging concept [15] presenting the advantage of preserving amplitude and phase of the scattering matrix over a rich frequency range. The potential drawback of such an approach is relatively high computation cost.

For these reasons, this paper focuses on developing an optimised and accelerated extraction of scattering features using the above-mentioned reversible imaging approach. Here, an image is first produced using the forward imaging method with full dynamic transmit-receive focusing. Then, the optimal-resolved image is spatially filtered according to a region of interest where scattering matrix extraction is desired. After that, the inverse imaging operation is performed in order to recover temporal responses corresponding to the scattered signals from the defect located in the selected region. Finally, the target scattering information is retrieved from the extracted local array data. Two implementations of this procedure are developed on a graphics processing unit (GPU), using delay-and-sum and frequency-wavenumber approaches [16], [17]. The performance of such implementations is evaluated in terms of accuracy, complexity, processing time, and hardware required. Also, optimal spatial windowing functions for the measurement of the scattering matrix are determined. This will

allow the optimal properties of scattering matrix extraction to be determined with a view to enabling detection and characterisation approaches reliant on its determination. The optimised extraction of scattering matrices is experimentally compared against the commonly used subarray approach.

This paper is organized as follows. Sec. II introduces the scattering matrix concept and the available methods for its extraction from the array data. Sec. III recalls the reversible back-propagation imaging method, which is exploited in this work. Sec. IV focuses on different implementations of the back-propagation method and points out the advantages and drawbacks of the suggested solutions. Finally, Sec. V presents different strategies for the optimal extraction of defect scattering matrices in granular structures using simulated and experimental data.

II. Extraction of the scattering matrix

The scattering matrix describes the acoustic properties resulting from the geometric properties of a scatterer in the far-field [18], [19]. The coefficients of this matrix provide the amplitude and phase of the scattered wave for a given incident plane wave.

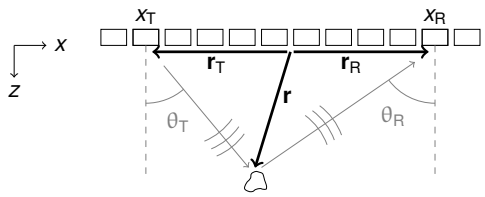

Fig. 1. Imaging array system.

Let us consider the diagram in Fig. 1. For a single mode, the full array data recorded using a linear array can be modelled in the frequency domain by

$$\begin{aligned} u(\mathbf{r}_\mathrm{T},\mathbf{r}_\mathrm{R},\omega) &= A(\omega)P(\mathbf{r}-\mathbf{r}_\mathrm{T},\omega) \\ &\quad \times S(\theta_\mathrm{T},\theta_\mathrm{R},\omega) \\ &\quad \times P(\mathbf{r}-\mathbf{r}_\mathrm{R},\omega), \end{aligned} \tag{1}$$

where A is the spectrum of the transmitted signal. P describes the propagation from a transmitter element at $\mathbf{r}_\mathrm{T}$ to the scatterer located at $\mathbf{r}$, and reciprocally from the scatterer to a receiver element at $\mathbf{r}_\mathrm{R}$, which can be defined as follows

$$P(\boldsymbol{\rho},\omega) = D(\boldsymbol{\rho},\omega)H_0^{(2)}(k\|\boldsymbol{\rho}\|)e^{-\alpha(\omega)\|\boldsymbol{\rho}\|}. \tag{2}$$

Here, D is the directivity function of an array element, $H_0^{(2)}$ is the Hankel function of the second kind, k is the wavenumber, and α is the attenuation coefficient. Finally, S is the scattering matrix which contains the complex scattering coefficients of the defect located at the position $\mathbf{r}$, and depends on the directions of incident and scattered waves (angles θ_T and θ_R).

In the NDT community, the dataset $u(\mathbf{r}_\mathrm{T},\mathbf{r}_\mathrm{R},t)$ is known as full matrix capture (FMC), and contains the temporal responses for all combinations of individual transmit and receive elements in the array. Due to reciprocity, this matrix is symmetric, and only the lower triangle elementary signals measured at positions $x_\mathrm{T} \leq x_\mathrm{R}$ are required for imaging or analysis. The acquisition containing all non redundant information in u is called half matrix capture (HMC).

In the particular case of an isolated scatterer, the associated scattering matrix can be directly measured from the array data by correcting the phase and the amplitude losses using Eq. (2). However, in many ultrasonic applications, the array data contain a superposition of signals, coming from surface waves, structural features, material microstructure (a particular challenge in NDT due to grain scattering), or other defects. To extract the target scattering matrix, those unwanted signals must be filtered. This section describes two techniques to reduce the contribution of undesirable information: a subarray approach [6], and a reversible imaging concept [15].

A. Subarray approach

The idea of the subarray approach is to focus on the target scatterer with a selected number of adjacent elements in transmission and in reception. In this case, due to the poor spatial selectivity, the scattering matrix cannot be calculated by simply inverting Eq. (2) and correcting the phase and amplitude losses in the frequency domain. Alternatively, a synthetic transmit-receive focusing using each sub-aperture is performed by summing the corresponding time-delayed target reflections. In practice, a narrow bandpass filter is applied to the array data in order to maximise the response at the frequency of interest. The procedure is summarised by the following equation [6]:

$$S_\mathrm{sub}(\theta_{\mathrm{T}(n)},\theta_{\mathrm{R}(m)},\omega_0) = \frac{\left|\sum_{\mathcal{T}_n}\sum_{\mathcal{R}_m} u_0\left(\mathbf{r}_\mathrm{T},\mathbf{r}_\mathrm{R},t=\frac{\|\mathbf{r}-\mathbf{r}_\mathrm{T}\|+\|\mathbf{r}-\mathbf{r}_\mathrm{R}\|}{c}\right)\right|}{\left|\sum_{\mathcal{T}_n}\sum_{\mathcal{R}_m} A(\omega_0)P(\mathbf{r}-\mathbf{r}_\mathrm{T},\omega_0)P(\mathbf{r}-\mathbf{r}_\mathrm{R},\omega_0)\right|}, \tag{3}$$

where c is the speed of sound, ω_0 is the centre angular frequency of the bandpass filter, u_0 is the narrow-band filtered array data, $\mathcal{T}_n$ and $\mathcal{R}_m$ denote the sets of elements in the n-th transmitter subarray and m-th receiver subarray, respectively; and $\theta_{\mathrm{T/R}(n)}$ is the angle of view from the center of the n-th subarray in direction to the scatterer located at $\mathbf{r}$. The expression in the denominator in Eq. (3) is the global amplitude correction due to the effects of array element directivity, beam spreading and attenuation.

The sub-aperture size is a key parameter for a reliable measure but remains an arbitrary empirical choice. There are two important factors, that need to be considered. First, larger sub-apertures provide better focusing power and enhance the spatial selectivity in comparison with individual elements. In this context, the choice of the sub-aperture size could be based on a fixed f-number which is defined as the ratio of the focal depth to the aperture size. For example, f-number of 1 means that the lateral resolution equals the wavelength. However, incident and scattered angles of the extracted scattering matrix are determined by the direction from the center of each sub-aperture to the center of the defect, and the corresponding scattering value represents an average over the angular range of the sub-aperture. Therefore, the sub-array approach acts as a

smoothing filter on the extracted scattering matrix and reduces its angular range.

Note that the coefficients of S_{sub} keep only the amplitude at ω_0 and lose all information related to the phase. In low-scattering materials, this is enough for the characterisation of defects such as voids, inclusions, or cracks. In materials with high grain scattering noise, amplitude and phase at multiple frequencies are needed for accurate characterisation, in particular while sizing defects [20]. For this reason, an alternative approach is required to access the multi-frequency scattering behaviour of defects.

B. Reversible imaging approach

The reversible imaging concept explores the fact that the imaging algorithm can be considered as a reversible transformation and allows recovery of the original array data from the array image [21], or a subregion of the image. The first step is to perform full dynamic focusing in transmission and reception, which converts the superposition of time traces into an image where the scatterers can be spatially localized. The main information about a scatterer resides in the vicinity of its location in the image. If the scatterer is spatially resolved, its temporal responses can be separated from the other scatterers present in the material. To this end, a spatial filter is applied on the image in order to isolate the scatterer of interest, then the associated local array data are extracted from the image by performing the inverse imaging operation.

Unlike the subarray approach, the target scatterer signals can be completely isolated. Thus, the scattering matrix can be estimated from the spectrum of the spatially filtered array data u_{rev} by

$$S_{\text{rev}}(\theta_{\text{T}}, \theta_{\text{R}}, \omega) = \frac{u_{\text{rev}}(\mathbf{r}_{\text{T}}, \mathbf{r}_{\text{R}}, \omega)}{A(\omega)P(\mathbf{r} - \mathbf{r}_{\text{T}}, \omega)P(\mathbf{r} - \mathbf{r}_{\text{R}}, \omega)}. \quad (4)$$

Here, S_{rev} contains amplitude and phase information across a range of frequencies.

III. Back-propagation imaging method

In this paper, the reversible imaging procedure discussed above is based on the back-propagation algorithm [15]. This method introduces the notion of a generalized image $g(x_{\text{T}}, x_{\text{R}}, z)$, which represents the full array data focused in transmission at (x_{T}, z), and in reception at (x_{R}, z). Note that when $x_{\text{T}} = x_{\text{R}}$, the focusing point is common in transmission and in reception, such as in the total focusing method (TFM) [3]. Indeed, the plane spanned by $x_{\text{T}} = x_{\text{R}}$ corresponds to a classic image produced by conventional beamformers, hence the terminology of generalized image. So, the classic image is given by

$$I(x, z) = g(x, x, z). \quad (5)$$

The extra information in the generalized image, where $x_{\text{T}} \neq x_{\text{R}}$, is essential for the reversible process.

A. Forward imaging

The back-propagation imaging method can be defined by a linear operator B that converts the full array data $u(x_{\text{T}}, x_{\text{R}}, t)$ into the generalized image:

$$g(x_{\text{T}}, x_{\text{R}}, z) = B\left[u(x_{\text{T}}, x_{\text{R}}, t)\right]. \quad (6)$$

The back-propagation operator is defined as a series of Fourier transforms, written as

$$B = F^{-1}MF, \quad (7)$$

where F and F^{-1} are the multidimensional direct and inverse Fourier transforms, respectively. Concisely, F transforms the data u from a spatio-temporal domain into a frequency-wavenumber domain:

$$U\left(k_{x_{\text{T}}}, k_{x_{\text{R}}}, \omega\right) = F[u(x_{\text{T}}, x_{\text{R}}, t)]. \quad (8)$$

Then, M maps the frequencies of the data into the wavenumbers k_z of the generalized image:

$$G\left(k_{x_{\text{T}}}, k_{x_{\text{R}}}, k_z(\omega)\right) = M[U\left(k_{x_{\text{T}}}, k_{x_{\text{R}}}, \omega\right)], \quad (9)$$

where

$$k_z = \sqrt{\frac{\omega^2}{c^2} - k_{x_{\text{T}}}^2} + \sqrt{\frac{\omega^2}{c^2} - k_{x_{\text{R}}}^2}. \quad (10)$$

Finally, F^{-1} transfers the angular spectrum G of the generalized image from the wavenumber domain into the spatial domain:

$$g(x_{\text{T}}, x_{\text{R}}, z) = F^{-1}[G\left(k_{x_{\text{T}}}, k_{x_{\text{R}}}, k_z(\omega)\right)]. \quad (11)$$

B. Inverse imaging

The invertibility of the back-propagation operator B allows recovery of the full array data from the generalized image:

$$u(x_{\text{T}}, x_{\text{R}}, t) = B^{-1}\left[g(x_{\text{T}}, x_{\text{R}}, z)\right], \quad (12)$$

where, the inverse imaging operator is defined by

$$B^{-1} = F^{-1}M^{-1}F. \quad (13)$$

Here, F transforms the generalized image into its angular spectrum G. Then, M^{-1} remaps the wavenumbers into the frequencies of the data. Finally, F^{-1} transforms the spectrum U from the frequency-wavenumber domain into the spatio-temporal domain. Thus the time series contribution from a region in space can be directly extracted.

The frequency-wavenumber formalism described in this section has been used in previous works to extract local array data. In particular, this paper introduces an alternative time domain technique, which is more common in array imaging and fully compatible with hardware and software of modern imaging systems. Both approaches represent a mathematically robust strategy to extract scattering information, however the details and optimisation of their implementation are key to the practical applicability of scattering matrix extraction and will be discussed next.

IV. Implementation of the back-propagation imaging

This section describes two implementations of the back-propagation method. The first approach exploits the computational efficiency of the fast Fourier transform (FFT) algorithm, and performs the migration in the frequency domain, as described in the previous section. The second approach uses a delay-and-sum (DAS) technique operating in the temporal domain, which is based on the asymptotic approximation of the back-propagation method (see Appendix A for a full description).

A. Fast Fourier transform approach

In this paper, the approach based on the application of Fourier transforms (as described in subsections III-A and III-B) is referred to as the FFT approach. Here, the fast computational speed of the discrete Fourier transform allows high imaging rates. However, the discrete implementation of the Fourier transform potentially leads to periodicity effects causing artefacts when the imaging range is reduced. In effect, all available time-traces in the data are mapped in the image even if they are associated with scatterers physically outside of the imaging range. This effect is commonly tackled by calculating the image on a large spatial domain in order to map the scatterers at their correct position. Essentially, producing a much larger image than the region of interest required. In addition to the potential periodicity issues, we must also consider the problem of artefacts resulting from the interpolation step following Eq. (10).

The Fourier transform operator F in Eq. (7) is performed using the tridimensional fast Fourier transform (3D-FFT) algorithm. Then, the angular spectrum G is obtained by interpolating the frequency-wavenumber array data U, in such a way as to avoid interpolation artefacts. To this end, every dimension, x_{T}, x_{R} and t, of the array data $u(x_{\mathrm{T}}, x_{\mathrm{R}}, t)$ is commonly padded with zeros in order to oversample the spectrum, at the cost of operation complexity and a significant memory space requirement. Alternatively, the extra memory cost can be reduced by using a sinc interpolator, also known as ideal interpolator, which is equivalent to the zero-padding operation translated to a convolution in frequency [22], [23]. While either of these approaches implemented correctly yields accurate results, the sinc interpolator is used in this paper in the ω domain due to its lower memory footprint. Zero-padding is still applied in the x_{T} and x_{R} directions to avoid multimensional sinc interpolations, where the latter could lead to an extremely high computation cost. This algorithmic choice is simple to implement, gives accurate migration results, and showed the best compromise between speed and memory among the possible FFT-based implementations. Once the migration is done, the operator F^{-1} is performed on the angular spectrum G using the tridimensional inverse fast Fourier transform (3D-IFFT) algorithm.

The implementation steps for the FFT based inverse imaging are the same as those for the forward imaging. First, the 3D-FFT is applied to the generalized image $g(x_{\mathrm{T}}, x_{\mathrm{R}}, z)$ converting it to the angular spectrum G, then the angular spectrum is interpolated using Eq. (10), and finally the 3D-IFFT is performed transforming the array data from the wavenumber-frequency $(k_{x_{\mathrm{T}}}, k_{x_{\mathrm{R}}}, \omega)$ domain to the spatio-temporal $(x_{\mathrm{T}}, x_{\mathrm{R}}, t)$ domain.

B. Delay-and-sum approach

DAS approaches are the most widely used in array imaging because of their robustness and ease of implementation. In these methods, times-of-flight from array elements to a focusing point are calculated in order to sum in phase all the set of signals. In this subsection, an implementation of back propagation imaging using DAS is explored, with the final equations of the forward and inverse operations provided. For further details of their derivation, see Appendix A.

1) DAS forward imaging: As mentioned before, in the generalized image $g(x_{\mathrm{T}}, x_{\mathrm{R}}, z)$, the array data are focused in transmission at $\mathbf{r}_{(\mathrm{T})} = \{x_{\mathrm{T}}, z\}^{\dagger}$, and in reception at $\mathbf{r}_{(\mathrm{R})} = \{x_{\mathrm{R}}, z\}^{\dagger}$. The contributions of every transmitter-receiver pair are then summed in phase using

$$g_{\mathrm{DAS}}(x_{\mathrm{T}}, x_{\mathrm{R}}, z) = \frac{-z^2}{2\pi c} \iint \frac{u_t\left(x'_{\mathrm{T}}, x'_{\mathrm{R}}, \frac{\|\mathbf{r}_{(\mathrm{T})} - \mathbf{r}'_{\mathrm{T}}\| + \|\mathbf{r}_{(\mathrm{R})} - \mathbf{r}'_{\mathrm{R}}\|}{c}\right)}{\|\mathbf{r}_{(\mathrm{T})} - \mathbf{r}'_{\mathrm{T}}\|^{\frac{3}{2}} \|\mathbf{r}_{(\mathrm{R})} - \mathbf{r}'_{\mathrm{R}}\|^{\frac{3}{2}}} dx'_{\mathrm{T}} dx'_{\mathrm{R}}, \tag{14}$$

where u_t is the derivative of u with respect to t.

2) DAS inverse imaging: The derivation of expressions for the inverse DAS imaging follows the same far-field approximations as for the forward DAS imaging. In the forward imaging (see Eq. (14)), the method extracts the amplitude of the transmitter-receiver signals at the instant t that is a function of the transmitter-receiver positions x_{T} and x_{R}, and the coordinates of the focusing point $(x'_{\mathrm{T}}, x'_{\mathrm{R}}, z)$. In the inverse imaging, the algorithm recovers the temporal signals by summing the generalized image intensities at the focusing depth z that is a function of coordinates x'_{T} and x'_{R} in the generalized image domain, and spatio-temporal coordinates $(x_{\mathrm{T}}, x_{\mathrm{R}}, t)$ of the array data. So, solving $t = (\|\mathbf{r}'_{(\mathrm{T})} - \mathbf{r}_{\mathrm{T}}\| + \|\mathbf{r}'_{(\mathrm{R})} - \mathbf{r}_{\mathrm{R}}\|)/c$ for z yields the following relationship

$$z = \frac{1}{2ct}\Big[c^4t^4 - 2c^2t^2\left((x_{\mathrm{T}} - x'_{\mathrm{T}})^2 + (x_{\mathrm{R}} - x'_{\mathrm{R}})^2\right) + \left((x_{\mathrm{R}} - x'_{\mathrm{R}})^2 - (x_{\mathrm{T}} - x'_{\mathrm{T}})^2\right)^2\Big]^{\frac{1}{2}}, \tag{15}$$

and the associated expression for the inverse imaging is given by

$$u_{\mathrm{DAS}}(x_{\mathrm{T}}, x_{\mathrm{R}}, t) = \frac{1}{2\pi c}\frac{d}{dt} \iint \frac{g\Big(x'_{\mathrm{T}}, x'_{\mathrm{R}}, z(x_{\mathrm{T}}, x_{\mathrm{R}}, x'_{\mathrm{T}}, x'_{\mathrm{R}}, t)\Big)}{\|\mathbf{r}'_{(\mathrm{T})} - \mathbf{r}_{\mathrm{T}}\|^{\frac{1}{2}} \|\mathbf{r}'_{(\mathrm{R})} - \mathbf{r}_{\mathrm{R}}\|^{\frac{1}{2}}} dx'_{\mathrm{T}} dx'_{\mathrm{R}}. \tag{16}$$

Note that the DAS back-propagation operator has to be performed for every set of three variables $(x_{\mathrm{T}}, x_{\mathrm{R}}, t)$, leaving the approach computationally inefficient. However, these far-field approximations do not present the periodicity effect, seen in the FFT approach. Therefore, the image can be calculated directly in the desired region of interest, without any additional zero-padding, since there is no need to expand

the imaging region. This leads to a significant reduction in memory requirements over the FFT approach.

The next subsection compares both implementations, FFT and DAS, discussing the imaging performance, the computational complexity, and the required memory size.

C. Implementation performances

For the initial comparison between the FFT and DAS implementations, only the forward imaging is considered. Since the computational performance of the inverse operators are the same as for the forward operator in each implementation, reliable conclusions about best practise may be drawn in this way.

1) Imaging: In the following comparison, the imaging configuration presented in Fig. 2 is considered. A 64-element array (0.5 mm pitch) with 2.5-MHz centre frequency (1-cycle pulse) imaging a 2-mm diameter through hole at 30 mm depth in a coarse grained material is simulated. The material properties, including grain size, are chosen similar to a copper sample used for experimental validation later in the paper. The mean grain size is 100 μm and the orthotropic material properties are $E_{11} = 168.6$ GPa, $E_{12} = 121.4$ GPa, $E_{44} = 75.4$ GPa and $\rho = 8960$ kg/m^3. The average longitudinal wave velocity is 4700 m/s yielding a wavelength of 1.88 mm. The full matrix capture is generated using a finite-element (FE) model implemented in the Pogo software package [24], [25]. The element edge length is 30 μm corresponding to a spatial sampling of 60 elements per wavelength. This investigation is carried out in FE to allow repeatable results where experimental variability can be completely eliminated in order to determine the best case performance of each approach.

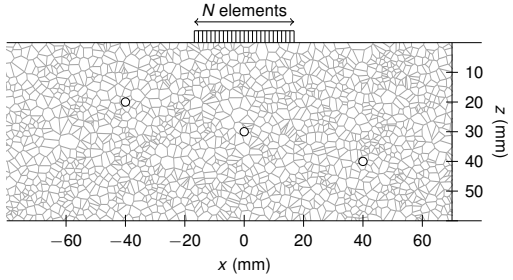

Fig. 2. Contact imaging configuration: a linear array of N elements is used to image and analyse a 2-mm side-drilled hole in a material with copper elastic properties.

Fig. 3 displays the back-propagated images $I(x, z)$ with an amplitude range of 40 dB for the FFT and DAS implementations. In the FFT case, inactive array elements were effectively placed at both sides of the real array (spatial zero-padding) to oversample the data spectrum and simultaneously cover a larger lateral imaging range. This allows the imaging artefacts previously discussed to be explored. The images are calculated in an extended area but displayed in a region just below the probe. When the imaging zone is not large enough, the FFT images present artefacts caused by reflectors that are periodically repeated in the lateral direction where the period equals the lateral size of the image, this can be seen in the changes in the images from Figs. 3(a)–(c). To limit this effect, an angular filter of 30° is applied to the angular spectrum array data U in the Fourier domain. However, even in this case, spatial zero-padding of factor 4 is still needed to achieve accurate artefact-free results. This leads to increased algorithmic complexity and computer memory required in the FFT method, which will be studied next. Contrary to the FFT approach, every imaging point in the DAS algorithm is independent, and thus any imaging region can be calculated without the imaging artefacts seen in the FFT approach. This can be seen in the good match between the oversampled FFT image and DAS image, Figs. 3(c) and (d) respectively. Having shown that the imaging performance is comparable, we will now explore the optimum approach in terms of memory demand and speed.

2) Memory: In the following, N is the number of array elements, N_t is the number of temporal samples, N_x is the number of sampling points in the lateral image dimension, and N_z is the number of sampling points in the z-direction of the image.

Table I summarizes the size of volumetric data needed to calculate the generalized image for FFT and DAS implementations, at each signal processing step. The only difference between the two approaches consists of the interpolation of the complex-valued spectrum in the FFT implementation, which represents a significant factor in terms of the required computer memory. As mentioned before, the migration in the FFT approach has to be performed using an accurate interpolation. The easiest method and common practice is to apply an extensive zero-padding, but this requires a significant memory space to hold the oversampled spectrum.

TABLE I
COMPARISON OF VOLUMETRIC DATA SIZES IN THE FFT AND DAS FORWARD IMAGING.

Volumetric data	FFT	DAS
$u(x_\mathrm{T}, x_\mathrm{R}, t)$	NNN_t	NNN_t
$U(k_{x_\mathrm{T}}, k_{x_\mathrm{R}}, \omega)$	$2N_xN_x(N_t/2+1)$	–
$G(k_{x_\mathrm{T}}, k_{x_\mathrm{R}}, k_z)$	$2N_xN_x(N_z/2+1)$	–
$g(x_\mathrm{T}, x_\mathrm{R}, z)$	$N_xN_xN_z$	$N_xN_xN_z$

Fig. 4(a) displays the memory requirements to execute the forward imaging algorithm in both cases. Here, $N_t = 512$, $N_z = 256$, and $N_x = 4N$ (to ensure no problems with periodicity), where the number of array elements is the variable N. Here the raw data were downsampled satisfying the Nyquist condition to minimise the number of temporal samples. The figure spans linear array sizes usually used in NDT, going from 32 to 128 elements, but also covers a 192-element array seen in medical ultrasonic imaging [26]. The memory is represented in gigabytes (GB) and is calculated considering single precision data. From that figure it is seen that the extra allocated data (spectra data U and G) exponentially increases the memory usage. In the case of $N = 128$, which is common in array imaging, more than 1 GB of memory must be allocated. This is feasible for offline processing on personal computers, but may be a limiting factor for portable imaging systems or if implemented on dedicated GPUs to increase processing

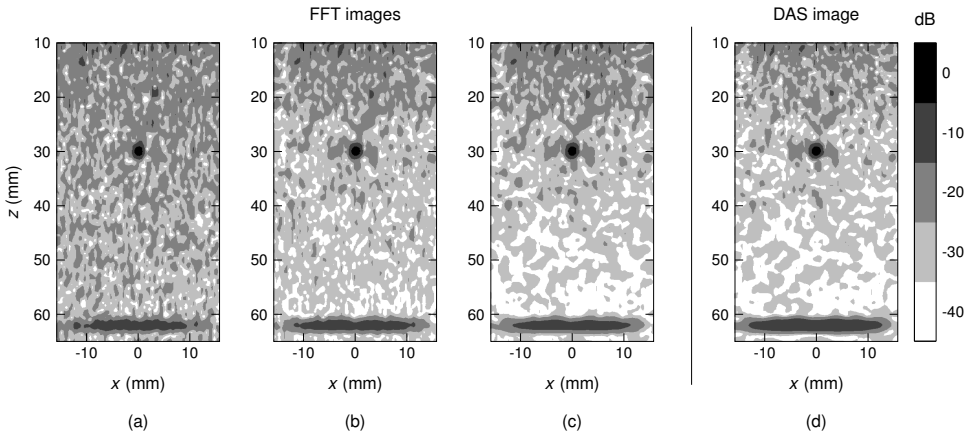

Fig. 3. Back-propagated images using FFT and DAS approaches zooming in the region below the probe. FFT calculated with a spatial zero-padding factor: (a) 1, (b) 2, and (c) 4. (d) DAS image directly calculated in the region displayed.

speed. In addition, if the area of imaging, or its resolution, is increased, this problem will only be magnified.

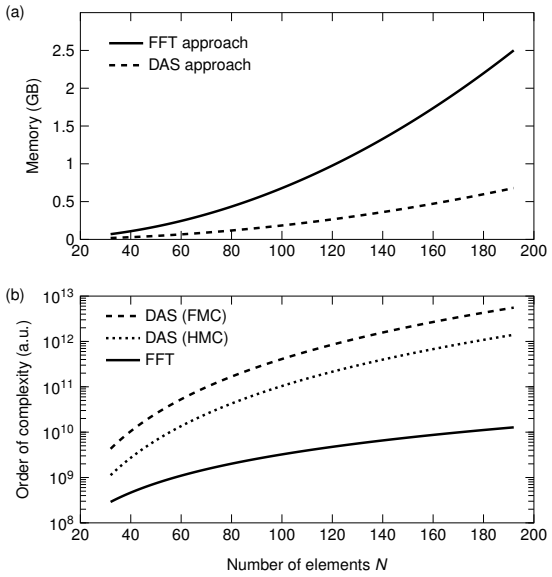

Fig. 4. Comparison of the forward imaging FFT and DAS implementations as a function of the number of elements N. (a) Total memory required in GB. (b) Algorithmic complexity using full matrix capture (FMC) and half matrix capture (HMC). Parameters used: $N_t = 512$, $N_z = 256$, and $N_x = 4N$.

3) Algorithmic complexity: The algorithmic complexities of the forward imaging at every stage are summarized in Table II. Here, C_{FFT} is the complexity coefficient corresponding to the interpolation performed in the frequency domain in order to transform angular spectrum from the angular frequency ω to the wavenumber k_z domain; and C_{DAS} represents the complexity factor of a linear interpolation in the time domain. Concerning the FFT approach, the complexity order is predominantly governed by the first 3D-FFT, since generally $N_t > N_z$ ($N_t \gg N_z$ if extensive zero-padding is applied in the time domain).

Fig. 4(b) illustrates the evolution of the complexity orders according to the number of array elements. For simplicity,

TABLE II
DESCRIPTION OF THE ALGORITHMIC COMPLEXITIES IN THE FFT AND DAS FORWARD IMAGING.

Stage	FFT	DAS
$u \to U$	$N_x N_x N_t \log_2(N_x N_x N_t)$	–
$U \to G$	$C_{\mathrm{FFT}} N_x N_x (N_z/2+1)$	–
$G \to g$	$N_x N_x N_z \log_2(N_x N_x N_z)$	–
$u \to g$	–	$C_{\mathrm{DAS}} N^2 N_x N_x N_z$

$C_{\mathrm{DAS}} = 1$ which is associated with a temporal linear interpolation, and $C_{\mathrm{FFT}} = 2$ when a complex linear interpolation is performed in the frequency domain. Note that for a large number of array elements, the computational gain in the FFT implementation is more than 100 in comparison with the DAS ones, using full or half matrix captures. This factor can be translated to a computation time gain which means that, in the same conditions, the FFT solution is 100 times faster than the DAS approach.

This study shows that the primary advantage of the DAS implementation resides in the low memory usage. However this does not take into account the added benefit that in the DAS approach the back-propagation can be calculated locally without artefacts, which reduces its computation time. Moreover, the acoustic reciprocity can be exploited to reduce this time by 2. This is because the symmetry of the generalized image relative to the main diagonal plane $x_{\mathrm{T}} = x_{\mathrm{R}}$, and the use of the half matrix capture. Also, an angular filter can be integrated (keeping constant f-number in the whole image) which reduces the number of operations and thus accelerates the DAS imaging rate. Each of these factors mean that for the application discussed here, of extracting multiple scattering matrices, the real world performance differential will be much smaller. This practical application is explored fully in the next section.

V. SCATTERING MATRIX EXTRACTORS BASED ON BACK-PROPAGATION

Scattering matrix extractors based on the FFT and DAS implementations of the back-propagation method were devel-

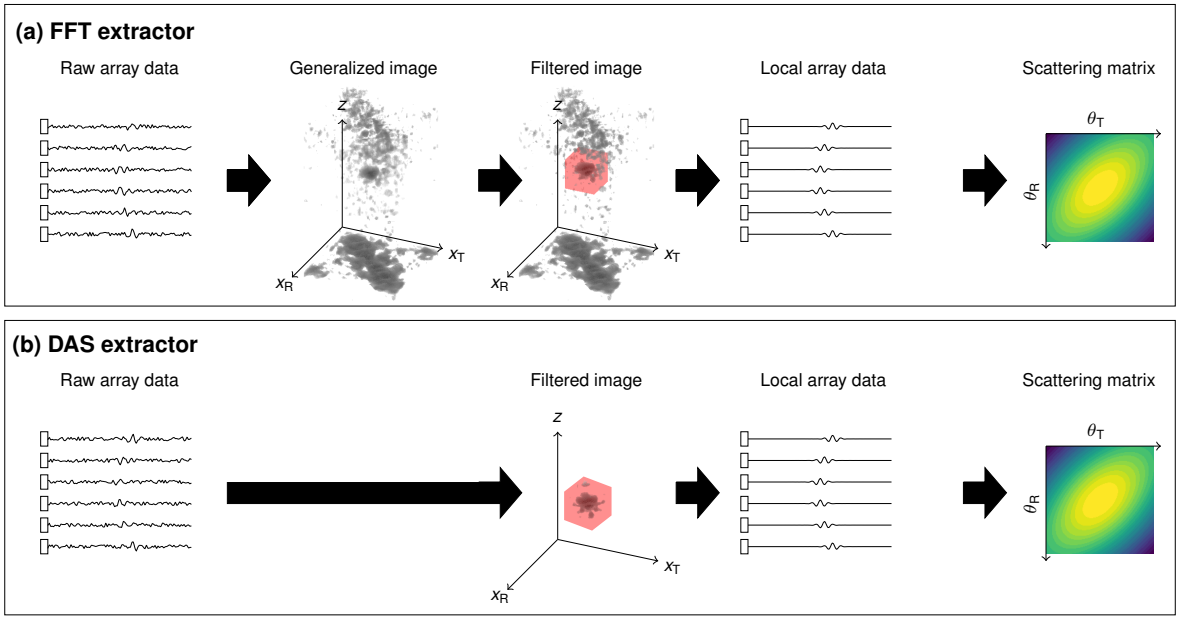

Fig. 5. Flowchart of the scattering matrix extraction using the back-propagation: (a) FFT, and (b) DAS procedures.

oped with the CUDA programming model and run on Matlab. This enables rapid computation of these readily parallelisable approaches to support the overall goal of fast scattering matrix extraction. The computer is a standard desktop with Intel Core i7-6700 CPU @3.4GHz (16 GB RAM) and an NVIDIA GPU GeForce GTX 1060 (6 GB RAM). The basic process applied in the FFT and DAS procedures to extract the scattering matrix from a region of interest are illustrated in Fig. 5.

In the FFT approach, the generalized image is calculated in an extended zone to avoid periodicity. Then, a spatial mask is used to isolate the region of interest. After that, the inverse imaging gives the local array data. Finally, the scattering matrix is calculated from these filtered data.

In the DAS approach, the generalized image is calculated only in the region of interest. Then, the associated time traces are recovered using the inverse operation in order to calculate the scattering matrix.

Here the DAS complexity is significantly reduced, in comparison with the results in the previous section, because only a small part of the generalized image is computed (skipping the first step in the FFT approach as seen in Fig. 5). In order to quantitatively illustrate this fact, the computation time of the whole procedure (forward imaging, inverse imaging, and scattering matrix calculation) is compared for different number of array elements N. The imaging configuration is the same as previously (see Fig. 2), but instead of calculating the whole image, the image domain is the region of interest defined by a $5{\times}5{\times}5$ mm^3 cuboid centred on the defect location.

Fig. 6 shows the evolution of the processing time and extraction rate by varying the number of array elements. For $N < 128$, both implementations give processing times below a hundred milliseconds. However, in terms of extraction rate, there is a noticeable difference between them, showing that in these conditions the DAS technique performs better. In particular, the DAS-HMC technique has overall the best performance since it requires low memory usage and is faster than the FFT approach. For example, when $N = 64$, the FFT based method extracts 30 scattering matrices per second, whereas the DAS-HMC algorithm gives the rate of 90 extracted scattering matrices per second. This highlights the computation time reductions inherent in the practical application of the DAS method, that is reduced imaging regions, as outlined in the previous section. It should be noted that the speed of the DAS method depends on the dimensions of the region of interest, so, for larger regions this technique could be much slower,

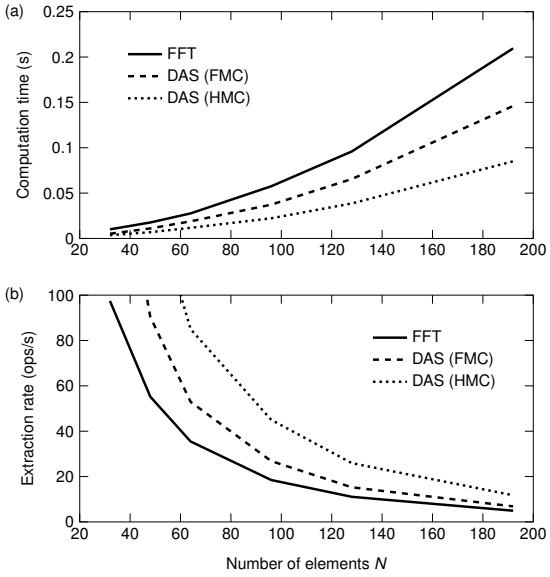

Fig. 6. (a) Computation time (in seconds) and (b) extraction rate (scattering matrices per second) of the FFT and DAS implementations as a function of the number of elements N.

but it represents an acceptable compromise between speed and memory.

One important point to mention is that these computation times correspond to the scattering matrix extraction from a single region of interest. If several positions need to be processed from the same array data, the FFT solution can be accelerated. To this end, the generalized image is calculated only once and held in memory, then the spatial filtering and inverse operation are performed for every region of interest in the retained image. This means that the computation time in the first step can be practically neglected and only the next steps have an effect in the extraction rate. Assuming that this is the case, the FFT approach gives similar rates as those in the DAS-FMC approach in this comparison.

Previous studies have validated the accurate extraction of the scattering matrix for different defects (holes and cracks with different orientations) in materials with low grain scattering noise using the back-propagation method [15], [27]. While an important step, the ability to measure scattering matrices in the presence of complex real world noise and scattering artefacts is key. As such the present work studies the extraction of defect scattering matrices in highly scattering materials. To this end, the local array datasets are extracted at 30 mm depth in the presence and absence of defects using simulated FE data (same array and material properties as described in the previous section). Fig. 7 allows us to compare visually the scattering matrices at 2.5 MHz obtained using both algorithms. The first row corresponds to a 2-mm side-drilled hole, the second row to a 2-mm horizontal crack, and the last one to the grain structure without defect. The theoretical scattering matrices of the defects were calculated using analytical scattering solutions for a cylindrical void [28] and a straight crack [29]. The scattering matrix of the grain noise was calculated by adding individual grain scattering responses based on a single scattering model [30], [31], described in Appendix B. This initial dataset was extracted using a cuboid region of interest as illustrated in Fig. 5. This will later be extended to investigate the optimum approach to mask the generalized image in order to extract accurate scattering matrices.

This comparison shows qualitatively that the scattering matrix shapes given by the FFT and DAS extractors are the same. The spatial filter reduces the grain scattering noise, but defect information is lost at large angles because of the spatial mask shape and the low signal to noise ratio. The high-amplitude information in the scattering matrix for the hole is located on the diagonal $\theta_{\mathrm{T}} = \theta_{\mathrm{R}}$ which contains the scattering coefficients in pulse-echo configuration; whereas the main information in the scattering matrix for the crack lies on the anti-diagonal which corresponds to the specular reflection. From the image, this discrimination between crack-like defect and void is not possible due to the sizes of the defects which are close to the wavelength. In the case of the structural noise, the measured matrices and the theoretical one exhibit the same anti-diagonal behaviour which is a key characteristic of the grain noise in the single scattering regime [32], [33]. This illustrates the clear benefit of using scattering matrices, specifically in a noisy environment.

In practice, as both approaches offer similar scattering coefficients, the choice of the extractor should be based on the trade-off between computation speed and memory requirements, and depends on the available computing hardware capabilities. For example, the hardware specifications used in this work allow large 3D-FFTs to be performed without memory issues and thus to produce very large images for most of the NDT linear array imaging applications, so here the speed of the FFT extractor is fully exploited, and it is the extractor used hereafter. In practical applications where either the available memory is limited or the region of interest is small, the DAS extractor is likely the preferred option.

In this example, the generalized image domain was filtered using a simple cuboid spatial filter to illustrate the scattering matrix extraction procedure. This has allowed the optimal extraction algorithm to be investigated. The next subsection investigates how to optimise the extracted scattering matrix, both in terms of the size of the spatial filter and its shape.

A. Spatial filtering in the generalized image

The spatial filtering in the generalized image is a crucial step for the extraction of the desired scattering features in the presence of noise and represents the final part of its optimisation. Here we investigate the optimisation of such a spatial filter. The following analysis is common to both the proposed extraction implementations since it is applied to the generalized image, so conclusions may be applied to either approach.

The generalized image can be approximated by the following convolution:

$$g(x_{\mathrm{T}}, x_{\mathrm{R}}, z) \approx o(x_{\mathrm{T}}, x_{\mathrm{R}}, z) * h(x_{\mathrm{T}}, x_{\mathrm{R}}, z), \qquad (17)$$

where $h(x_{\mathrm{T}}, x_{\mathrm{R}}, z)$ is the generalized point spread function, and $o(x_{\mathrm{T}}, x_{\mathrm{R}}, z)$ is the object function (reflectivity map) in the generalized space. The point spread function describes the spatial response of the array when a point-like scatterer is located at (x_0, z_0) in the conventional plane x-z [34], [35]. In this case the object function is defined as $o(x_{\mathrm{T}}, x_{\mathrm{R}}, z) = \delta(x_{\mathrm{T}} - x_0, x_{\mathrm{R}} - x_0, z - z_0)$, where δ is the delta function.

Recently, the generalized point spread function for a scatterer centred below the probe has been fully described [21]. The main side lobes are located in the x_{T}-z and x_{R}-z planes, and the analytical expressions of their amplitude have been developed. This result can be used to design an adapted filtering mask for defects with sizes comparable to the ultrasonic wavelength λ_0. For larger defects, the expected response in the generalized image domain can be calculated using the expression in Eq. (17). However, the signature of the point spread function may dramatically differ from one position to another. Thus, the point spread function has to be calculated for every region of interest, which is not a major concern thanks to the high imaging rate of the suggested implementations. Another solution is to precompute the point spread functions at strategically chosen positions in order to cover most of the imaging space [36].

Fig. 8 displays the generalized point spread function when an isolated ideal point scatterer is centred below the array at the depth of 30 mm (64-element array at 2.5 MHz). The

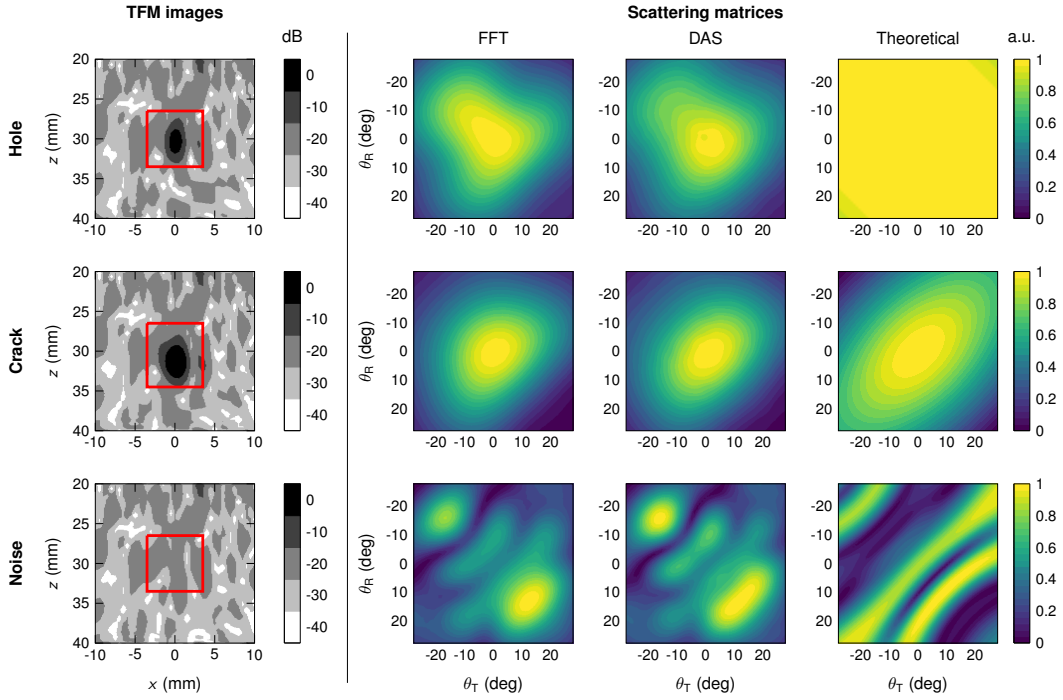

Fig. 7. The left panel shows the TFM images at 2.5 MHz obtained for different cases (sample with a hole and crack located at 30 mm depth, and defect-free material) using an array of 64 elements with 0.5 mm-pitch. The right panel presents the associated scattering matrices corresponding to the region of interest shown as a red square area on the TFM images (FFT and DAS approaches, and theoretical solutions).

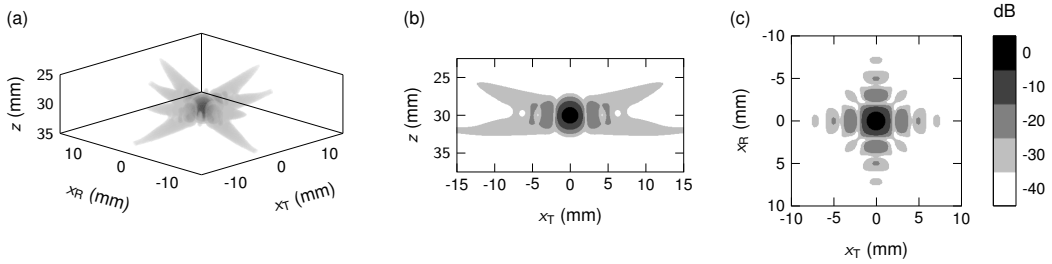

Fig. 8. Generalized point spread function at 30 mm depth. (a) Representation in the generalized space x_{T}-x_{R}-z; (b) slice in the plane x_{T}-z when $x_{\mathrm{R}} = 0$; (c) slice in the plane x_{T}-x_{R} when $z = 30$ mm.

suggested spatial mask is based on the region covered by the point spread function at a given amplitude level. For example, the associated mask at a –30 dB level is defined by the faces of the volume in Fig. 8(a). The mask amplitude level can be chosen according to the signal to noise ratio in the image.

To assess the effect of such spatial filtering, the generalized image is first calculated in a cuboid of dimensions $L \times L \times L$ centred at the defect location using the FE data described earlier in this section. Then, the scattering matrices are extracted using the full volume and also when a mask at –25 dB is applied. To quantify the extraction performance, a correlation score between extracted scattering matrices and the theoretical defect scattering matrix is calculated [37]. Fig. 9 shows the similarity scores as a function of the box size, for a hole and for a crack. In both cases, the maximal score lies close to 2.5 wavelengths which corresponds to the box size used in the previous subsection ($5{\times}5{\times}5$ mm^3). Beyond this size, the full volume introduces more noise than defect information. On the other hand, larger boxes with the mask preserve signal information without introducing noise. After the size of the box L reaches the lateral extent of the mask at –25 dB, which is about six wavelengths, the spatial filtering mask has reached its maximum extent and remains the same.

Fig. 10 shows the scattering matrices extracted when $L = 10$ mm (about 5 wavelengths) to qualitatively compare the masking effect. Using the full volume, the presence of noise is visible in the scattering matrix, but defect information is still present allowing the similarity metric to clearly distinguish the defect (hole and crack) from the noise. This is in contrast to the masked version where only the defect remains. For characterisation purposes, the use of the mask is a more appropriate option as it provides defect scattering coefficients over a large angular range.

Because of the size of defects tested here, their behaviour in the generalized image is very similar and follows the pattern of the point spread function. In ideal circumstances, the proposed mask filter allows the recovery of the focused information of a small reflector by recovering complementary scattering

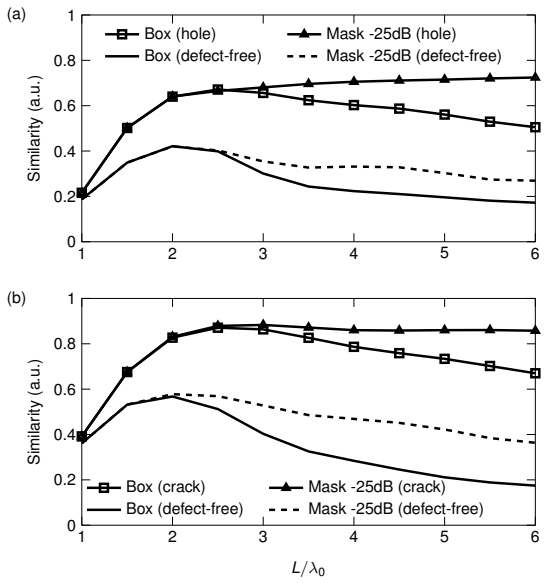

Fig. 9. Similarity between the expected scattering matrix of the target defect and the extracted ones from a cuboid of dimensions $L \times L \times L$ using the full volume and masked by the point spread function faces at –25 dB: (a) 2-mm diameter hole, and (b) 2-mm horizontal crack.

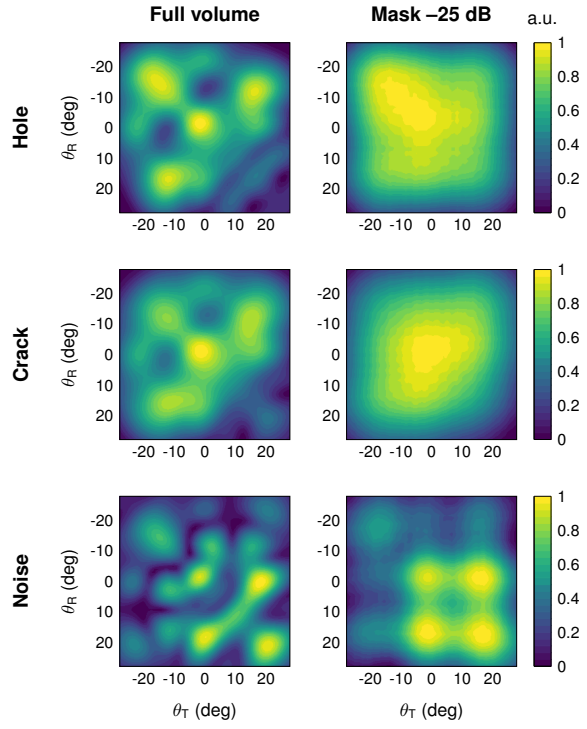

Fig. 10. Scattering matrices extracted from a cuboid of dimensions $10\times10\times10$ mm^3: Full volume (left column), and masked by the point spread function at –25 dB (right column). Cases: hole, crack, and defect-free.

information at the main lobes. However, practically in most conditions the box shaped spatial filter is the best option. The shape of the mask changes significantly across the image space and with the type of defect studied, thus an optimised (2.5-wavelength-sized) box filter represents the best solution in most conditions.

B. Experimental evaluation of the subarray and back-propagation extractors

In the previous subsection, the reliability of the scattering matrix extraction using the back-propagation method has been demonstrated. The subarray approach has been largely used over the last decade for the extraction of scattering features and has given accurate results, but typically in materials with low levels of grain scattering noise. In this subsection, the proposed extractor is compared against the subarray approach in the cases of low and high grain scattering noise using experimental data. This is key for use in real world engineering materials and is used to investigate the effect of multiple scattering on the developed scattering matrix extraction approaches.

The experimental set-up is the same as described in Fig. 2, but the specimen is a copper sample rather than a numerical simulation. A 64-element array (0.5 mm element pitch), operating at 5 MHz with a 60% fractional bandwidth at -6 dB is used. The aim here is to validate the scattering matrix extraction for a 2-mm side-drilled hole at 30 mm depth in the single and multiple scattering regimes. The level of multiple scattering can be controlled by applying different frequency filters to the array data before imaging in order to determine the relative robustness of the different scattering matrix extraction methods.

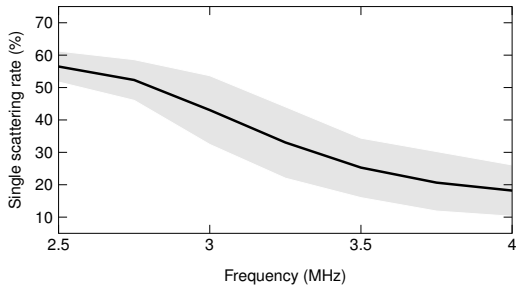

Fig. 11. Single scattering rate at 30 mm depth in the copper sample. The shaded region represents one standard deviation from the mean of different realizations.

The single scattering rate can be estimated from the specific properties of the generalized image [38]. The main contribution from single scattering is located around the main diagonal of the generalized image (when $x_{\mathrm{T}} = x_{\mathrm{R}}$). Contrary to this, the multiple scattering contribution is spread over the whole generalized image. Note that this property means that appropriate spatial filtering in the generalized imaging space can significantly reduce multiple scattering noise in the extracted data. This means that the developed back-propagation approach will be more robust to the presence of multiple scattering than the subarray approach. The single scattering rate as a function of frequency is shown in Fig. 11 for the copper sample. It can be seen that at this depth, the copper sample exhibits a high rate of multiple scattering, greater than 50% of the total image intensity, above approximately 3 MHz.

To assess the extraction robustness, scattering matrices are measured using the subarray approach (8-element subaperture [6]) and the optimised back-propagation method, in the presence and absence of a defect. Similarity scores between these

matrices and the expected theoretical scattering matrix of a hole are calculated for different frequencies, as seen in Fig. 12. At relatively low frequencies, both algorithms are able to resolve the scattering features of the hole from the background noise, although the back-propagation method gives a higher correlation coefficient than the subarray approach as a result of the averaging inherent in the subarray method and spatial filtering in the generalized imaging domain. This becomes particularly important and apparent at higher frequencies, when the multiple scattering noise increases. For example, at 4 MHz, the scattering matrix extracted using the subarray approach behaves as noise, while that extracted using the back-propagation method preserves defect information.

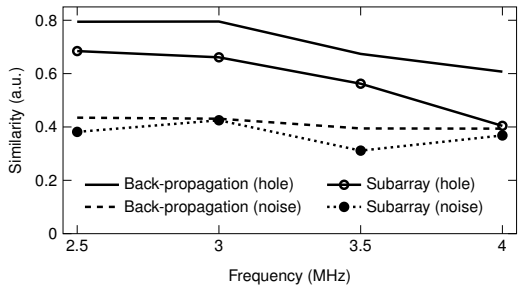

Fig. 12. Similarity between the expected scattering matrix of a hole and the extracted ones using the subarray approach and the back-propagation.

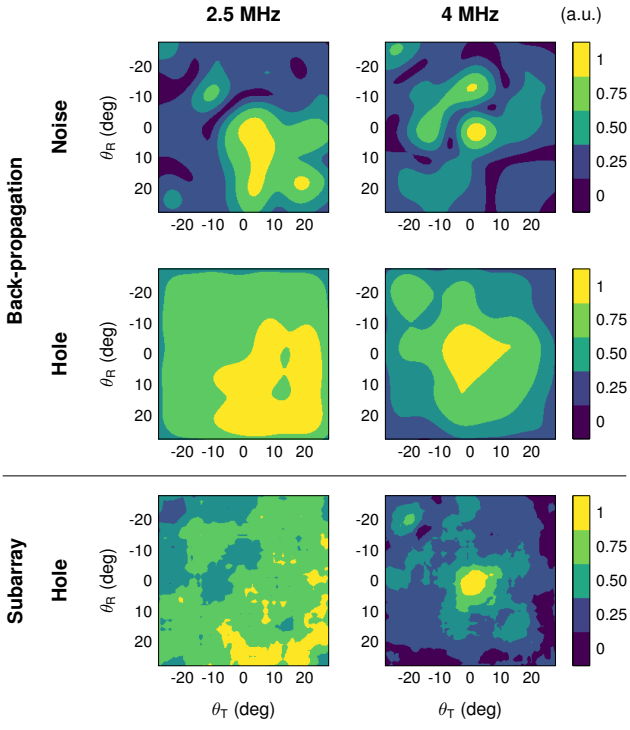

Fig. 13. Experimental scattering matrices measured using the subarray and back-propagation extractors.

Fig. 13 displays the scattering matrices at 2.5 MHz (low multiple scattering rate) and 4 MHz (high multiple scattering rate). The back-propagation gives uniform scattering coefficients as expected for a hole, while showing significant variability in the noise response. Qualitatively and quantitatively, the back-propagation extractor performs better than the subarray approach and is more suitable for characterisation in grainy materials since it provides amplitude and phase information over a broad frequency range.

VI. Conclusion

In this work, the reversible back-propagation method is used to extract scattering features in highly scattering materials. The imaging algorithm is presented in its integral form (FFT approach) and in its asymptotic expression (DAS approach). These strategies are optimised in a parallel implementation achieving high extraction rates. For example, using a 64-element array, at least 30 scattering matrices can be extracted per second. This is suitable for massive offline processing, or for real-time characterisation. In particular, the DAS approach is more convenient for limited-memory embedded systems giving the same accuracy and rates as the FFT approach. Each of these approaches are well suited to spatial filtering in the generalized imaging domain. Either using an optimised box size to minimise the contribution from noise, or using a mask derived from the point spread function. Although the latter offers marginally better performance, practical considerations mean that its application is significantly more complex, so in general the box mask is a better solution. Besides the speed, the proposed strategies provide a rich frequency spectrum of the scattering matrix, preserve phase information and are readily suited to minimising the effects of structural scattering noise.

The access to the scattering coefficients is only one of a diverse range of applications. In effect, the power of the proposed method is based on the possibility of the rapid extraction of the local array data, which could be post-processed for different purposes. For example, additional signal processing might include imaging enhancement via eigendecomposition of the time reversal operator [39], [40], or to estimate the rate of single and multiple scattering in the data [38].

Appendix A
Asymptotic Expressions of the Reversible Back-Propagation Method

In this appendix, the expressions of the DAS forward and inverse imaging are derived from the integral form of the back-propagation method using an asymptotic development [41].

A. Time-domain forward imaging

The generalized image calculation is thoroughly described by [15]:

$$g(x_{\mathrm{T}}, x_{\mathrm{R}}, z) = \frac{1}{(2\pi)^3} \int u(x'_{\mathrm{T}}, x'_{\mathrm{R}}, \omega) e^{jk_{x_{\mathrm{T}}}(x_{\mathrm{T}} - x'_{\mathrm{T}})} \times e^{jk_{x_{\mathrm{R}}}(x_{\mathrm{R}} - x'_{\mathrm{R}})} e^{jk_z z} \times dx'_{\mathrm{T}} dx'_{\mathrm{R}} dk_{x_{\mathrm{T}}} dk_{x_{\mathrm{R}}} d\omega, \quad (18)$$

where $k_z = \sqrt{k^2 - k_{x_{\mathrm{T}}}^2} + \sqrt{k^2 - k_{x_{\mathrm{R}}}^2}$.

A convenient reordering of the integrals in the previous equation yields

$$g(x_{\mathrm{T}},x_{\mathrm{R}},z)=\frac{1}{(2\pi)^3}\int\int e^{j(k_{x_{\mathrm{T}}}(x_{\mathrm{T}}-x'_{\mathrm{T}})+z\sqrt{k^2-k^2_{x_{\mathrm{T}}}})}dk_{x_{\mathrm{T}}} \times\int e^{j(k_{x_{\mathrm{R}}}(x_{\mathrm{R}}-x'_{\mathrm{R}})+z\sqrt{k^2-k^2_{x_{\mathrm{R}}}})}dk_{x_{\mathrm{R}}} \times u(x'_{\mathrm{T}},x'_{\mathrm{R}},\omega)dx'_{\mathrm{T}}dx'_{\mathrm{R}}d\omega. \quad (19)$$

The two inner integrals can be asymptotically approximated using

$$\int e^{j(k_x x+z\sqrt{k^2-k_x^2})}dk_x\approx\frac{\sqrt{-j2\pi k}z}{R^{3/2}}e^{jkR}, \quad (20)$$

where $R=\sqrt{x^2+z^2}$. By doing so, the expression of the generalized image becomes

$$g(x_{\mathrm{T}},x_{\mathrm{R}},z)\approx\frac{1}{(2\pi)^3}\int\frac{-j2\pi kz^2}{R_{\mathrm{T}}^{3/2}R_{\mathrm{R}}^{3/2}}u(x'_{\mathrm{T}},x'_{\mathrm{R}},\omega) \times e^{jk(R_{\mathrm{T}}+R_{\mathrm{R}})}dx'_{\mathrm{T}}dx'_{\mathrm{R}}d\omega. \quad (21)$$

Finally, the DAS imaging method is obtained by calculating the inverse Fourier transform over the frequencies, which is

$$g_{\mathrm{DAS}}(x_{\mathrm{T}},x_{\mathrm{R}},z)= \frac{-1}{2\pi c}\iint\frac{z^2}{R_{\mathrm{T}}^{3/2}R_{\mathrm{R}}^{3/2}}u_t\left(x'_{\mathrm{T}},x'_{\mathrm{R}},t=\frac{R_{\mathrm{T}}+R_{\mathrm{R}}}{c}\right)dx'_{\mathrm{T}}dx'_{\mathrm{R}}, \quad (22)$$

where u_t is the derivative of u with respect to t.

B. Time-domain inverse imaging

The inverse operation is given by [15]:

$$u(x_{\mathrm{T}},x_{\mathrm{R}},t)=\frac{1}{(2\pi)^3}\int g(x'_{\mathrm{T}},x'_{\mathrm{R}},k_z)e^{jk_{x_{\mathrm{T}}}(x_{\mathrm{T}}-x'_{\mathrm{T}})} \times e^{jk_{x_{\mathrm{R}}}(x_{\mathrm{R}}-x'_{\mathrm{R}})}e^{j\omega t} \times dx'_{\mathrm{T}}dx'_{\mathrm{R}}dk_{x_{\mathrm{T}}}dk_{x_{\mathrm{R}}}dk_z, \quad (23)$$

where

$$\omega=\frac{\sqrt{k_z^4+2k_z^2(k_{x_{\mathrm{R}}}^2+k_{x_{\mathrm{T}}}^2)+\left(k_{x_{\mathrm{R}}}^2-k_{x_{\mathrm{T}}}^2\right)^2}}{2k_z/c}, \quad (24)$$

which is the inverse of k_z with respect to ω.

The previous equation can be conveniently reorganised as

$$u(x_{\mathrm{T}},x_{\mathrm{R}},t)= \frac{1}{(2\pi)^3}\int\iint e^{j(k_{x_{\mathrm{T}}}(x_{\mathrm{T}}-x'_{\mathrm{T}})+k_{x_{\mathrm{R}}}(x_{\mathrm{R}}-x'_{\mathrm{R}})+\omega t)}dk_{x_{\mathrm{T}}}dk_{x_{\mathrm{R}}} \times g(x'_{\mathrm{T}},x'_{\mathrm{R}},k_z)dx'_{\mathrm{T}}dx'_{\mathrm{R}}dk_z. \quad (25)$$

The double inner integral is asymptotically evaluated yielding

$$\iint e^{j(k_{x_{\mathrm{T}}}(x_{\mathrm{T}}-x'_{\mathrm{T}})+k_{x_{\mathrm{R}}}(x_{\mathrm{R}}-x'_{\mathrm{R}}))} \times e^{\frac{jct}{2k_z}\sqrt{k_z^4+2k_z^2(k_{x_{\mathrm{R}}}^2+k_{x_{\mathrm{T}}}^2)+\left(k_{x_{\mathrm{R}}}^2-k_{x_{\mathrm{T}}}^2\right)^2}}dk_{x_{\mathrm{T}}}dk_{x_{\mathrm{R}}} \approx\frac{j2\pi\sqrt{R_{\mathrm{T}}R_{\mathrm{R}}}}{(R_{\mathrm{T}}+R_{\mathrm{R}})\zeta}k_z e^{jk_z\zeta} \quad (26)$$

where $R_{\mathrm{T/R}}=\sqrt{(x_{\mathrm{T/R}}-x'_{\mathrm{T/R}})^2+\zeta^2}$ and

$$\zeta=\frac{1}{2ct}\Big[c^4t^4-2c^2t^2\left((x_{\mathrm{T}}-x'_{\mathrm{T}})^2+(x_{\mathrm{R}}-x'_{\mathrm{R}})^2\right) +\left((x_{\mathrm{R}}-x'_{\mathrm{R}})^2-(x_{\mathrm{T}}-x'_{\mathrm{T}})^2\right)^2\Big]^{\frac{1}{2}}. \quad (27)$$

Note that previous expression is the inverse of $t=(R_{\mathrm{T}}+R_{\mathrm{R}})/c$ with respect to ζ.

This approximation leads to

$$u(x_{\mathrm{T}},x_{\mathrm{R}},t)\approx\frac{1}{(2\pi)^3}\int\frac{j2\pi\sqrt{R_{\mathrm{T}}R_{\mathrm{R}}}}{(R_{\mathrm{T}}+R_{\mathrm{R}})\zeta}k_z g(x'_{\mathrm{T}},x'_{\mathrm{R}},k_z) \times e^{jk_z\zeta}dx'_{\mathrm{T}}dx'_{\mathrm{R}}dk_z. \quad (28)$$

Finally, the inverse Fourier transform over k_z gives the expression of the inverse DAS operator:

$$u_{\mathrm{DAS}}(x_{\mathrm{T}},x_{\mathrm{R}},t)= \frac{1}{2\pi}\iint\frac{\sqrt{R_{\mathrm{T}}R_{\mathrm{R}}}}{(R_{\mathrm{T}}+R_{\mathrm{R}})\zeta}g_z(x'_{\mathrm{T}},x'_{\mathrm{R}},z=\zeta)dx'_{\mathrm{T}}dx'_{\mathrm{R}}, \quad (29)$$

where g_z is the derivative of g with respect to z.

Alternatively, the previous equation can be expressed as

$$u_{\mathrm{DAS}}(x_{\mathrm{T}},x_{\mathrm{R}},t)= \frac{1}{2\pi c}\frac{d}{dt}\iint\frac{1}{\sqrt{R_{\mathrm{T}}R_{\mathrm{R}}}}g(x'_{\mathrm{T}},x'_{\mathrm{R}},z=\zeta)dx'_{\mathrm{T}}dx'_{\mathrm{R}}. \quad (30)$$

APPENDIX B
SCATTERING MATRIX OF GRAIN NOISE

This appendix describes the formulation of the theoretical scattering matrix of grain noise in a single scattering assumption. In this simplified model, every grain is considered as a point-like scatterer with a given amplitude, which could be related to the size or orientation of the physic grain.

The far-field expression of the grain scattering matrix is given by the superposition of individual responses:

$$S(\theta_{\mathrm{T}},\theta_{\mathrm{R}},\omega)=\sum_{n=1}^{N_{\mathrm{g}}}a_n e^{jk(\mathbf{e}_{\theta_{\mathrm{T}}}+\mathbf{e}_{\theta_{\mathrm{R}}})\cdot\mathbf{r}_n}, \quad (31)$$

where N_{g} is the number of scatterers uniformly distributed in a region of interest at positions $\mathbf{r}_n=\{x_n,z_n\}^\dagger$. The amplitudes a_n of these scatterers follow a centred normal distribution, whose standard deviation is adjusted in order to have the same single scattering behaviour as a given polycrystalline material [30]. Finally, $\mathbf{e}_{\theta_{\mathrm{T}}}=\{\sin\theta_{\mathrm{T}},\cos\theta_{\mathrm{T}}\}^\dagger$ is the unit vector in direction to the n-th point-like scatterer, and $\mathbf{e}_{\theta_{\mathrm{R}}}=\{\sin\theta_{\mathrm{R}},\cos\theta_{\mathrm{R}}\}^\dagger$ is the unit vector of the associated scattered wave.

REFERENCES

[1] R. Y. Chiao and L. J. Thomas, "Analytic evaluation of sampled aperture ultrasonic imaging techniques for NDE," *IEEE Trans. Ultrason., Ferroelectr., Freq. Control*, vol. 41, no. 4, pp. 484–493, 1994.

[2] C. Prada and J.-L. Thomas, "Experimental subwavelength localization of scatterers by decomposition of the time reversal operator interpreted as a covariance matrix," *J. Acoust. Soc. Am.*, vol. 114, no. 1, pp. 235–243, 2003.

[3] C. Holmes, B. W. Drinkwater, and P. D. Wilcox, "Post-processing of the full matrix of ultrasonic transmit-receive array data for non-destructive evaluation," *NDT&E Int.*, vol. 38, no. 8, pp. 701–711, 2005.

[4] N. Portzgen, D. Gisolf, and G. Blacquiere, "Inverse wave field extrapolation: a different NDI approach to imaging defects," *IEEE Trans. Ultrason., Ferroelectr., Freq. Control*, vol. 54, no. 1, pp. 118–127, 2007.

[5] A. J. Hunter, , B. W. Drinkwater, and P. D. Wilcox, "The wavenumber algorithm for full-matrix imaging using an ultrasonic array," *IEEE Trans. Ultrason., Ferroelectr., Freq. Control*, vol. 55, no. 11, pp. 2450–2462, 2008.

[6] J. Zhang, B. W. Drinkwater, and P. D. Wilcox, "Defect characterization using an ultrasonic array to measure the scattering coefficient matrix," *IEEE Trans. Ultrason., Ferroelectr., Freq. Control*, vol. 55, no. 10, pp. 2254–2265, 2008.

[7] A. Velichko, L. Bai, and B. W. Drinkwater, "Ultrasonic defect characterization using parametric-manifold mapping," *Proc. Royal Soc. A: Math., Phys. and Eng. Sc.*, vol. 473, no. 2202, 2017, proc. Royal Soc. A: Math., Phys. and Eng. Sc.

[8] A. Fidahoussen, P. Calmon, M. Lambert, S. Paillard, and S. Chatillon, "Imaging of defects in several complex configurations by simulation-helped processing of ultrasonic array data," in *AIP Conference Proceedings*, vol. 1211, no. 1, 2010, pp. 847–854.

[9] K. Sy, P. Brédif, E. Iakovleva, O. Roy, and D. Lesselier, "Development of the specular echoes estimator to predict relevant modes for total focusing method imaging," *NDT&E Int.*, vol. 99, pp. 134–140, 2018.

[10] L. Merabet, S. Robert, and C. Prada, "The multi-mode plane wave imaging in the fourier domain: Theory and applications to fast ultrasound imaging of cracks," *NDT&E Int.*, vol. 110, 2020.

[11] J. Camacho, D. Atehortua, J. F. Cruza, J. Brizuela, and J. Ealo, "Ultrasonic crack evaluation by phase coherence processing and TFM and its application to online monitoring in fatigue tests," *NDT&E Int.*, vol. 93, pp. 164–174, 2018.

[12] M. V. Felice and Z. Fan, "Sizing of flaws using ultrasonic bulk wave testing: A review," *Ultrasonics*, vol. 88, pp. 26–42, 2018.

[13] J. B. Elliott, M. J. S. Lowe, P. Huthwaite, R. Phillips, and D. J. Duxbury, "Sizing subwavelength defects with ultrasonic imagery: An assessment of super-resolution imaging on simulated rough defects," *IEEE Trans. Ultrason., Ferroelectr., Freq. Control*, vol. 66, no. 10, pp. 1634–1648, 2019.

[14] N. Laroche, S. Bourguignon, E. Carcreff, J. Idier, and A. Duclos, "An inverse approach for ultrasonic imaging from full matrix capture data: Application to resolution enhancement in NDT," *IEEE Trans. Ultrason., Ferroelectr., Freq. Control*, vol. 67, no. 9, pp. 1877–1887, 2020.

[15] A. Velichko and P. D. Wilcox, "Reversible back-propagation imaging algorithm for postprocessing of ultrasonic array data," *IEEE Trans. Ultrason., Ferroelectr., Freq. Control*, vol. 56, no. 11, pp. 2492–2503, 2009.

[16] D. Garcia, L. Le Tarnec, S. Muth, E. Montagnon, J. Porée, and G. Cloutier, "Stolt's f-k migration for plane wave ultrasound imaging," *IEEE Trans. Ultrason., Ferroelectr., Freq. Control*, vol. 60, no. 9, pp. 1853–1867, 2013.

[17] L. Merabet, S. Robert, and C. Prada, "2-D and 3-D reconstruction algorithms in the fourier domain for plane wave imaging in non-destructive testing," *IEEE Trans. Ultrason., Ferroelectr., Freq. Control*, vol. 66, no. 4, pp. 772–788, 2019.

[18] L. Flax, L. R. Dragonette, and H. Überall, "Theory of elastic resonance excitation by sound scattering," *J. Acoust. Soc. Am.*, vol. 63, no. 723, pp. 723–731, 1978.

[19] L. W. Schmerr Jr., *Fundamentals of Ultrasonic Nondestructive Evaluation: A Modeling Approach*. New York: Springer, 2016.

[20] L. Bai, A. Velichko, and B. W. Drinkwater, "Ultrasonic defect characterisation–Use of amplitude, phase, and frequency information," *J. Acoust. Soc. Am.*, vol. 143, no. 1, pp. 349–360, 2018.

[21] A. Velichko and A. J. Croxford, "Strategies for data acquisition using ultrasonic phased arrays," *Proc. Royal Soc. A: Math., Phys. and Eng. Sc.*, vol. 474, no. 2218, 2018.

[22] J. H. Rosenbaum and G. F. Boudreaux, "Rapid convergence of some seismic processing algorithms," *Geophysics*, vol. 46, no. 12, pp. 1667–1672, 1981.

[23] R. H. Stolt and A. B. Weglein, *Seismic Imaging and Inversion: Application of Linear Inverse Theory*. Cambridge University Press, 2012, vol. 1.

[24] P. Huthwaite, "Accelerated finite element elastodynamic simulations using the GPU," *J. Comput. Phys.*, vol. 257, Part A, pp. 687–707, 2014.

[25] H. A. Bloxham, A. Velichko, and P. D. Wilcox, "Establishing the limits of validity of the superposition of experimental and analytical ultrasonic responses for simulating imaging data," *IEEE Trans. Ultrason., Ferroelectr., Freq. Control*, vol. 66, no. 1, pp. 101–108, 2019.

[26] J. A. Jensen, *Imaging of Complex Media with Acoustic and Seismic Waves*, ser. Topics in Applied Physics. Springer-Verlag Berlin Heidelberg, 2002, vol. 84, ch. Ultrasound imaging and its modeling, pp. 135–166.

[27] J. Zhang, B. W. Drinkwater, and P. D. Wilcox, "The use of ultrasonic arrays to characterize crack-like defects," *J. NDE*, vol. 29, no. 4, pp. 222–232, 2010.

[28] A. L. Lopez-Sanchez, H.-J. Kim, L. W. Schmerr Jr., and A. Sedov, "Measurement models and scattering models for predicting the ultrasonic pulse-echo response from side-drilled holes," *J. NDE*, vol. 24, no. 3, pp. 83–95, 2005.

[29] E. Glushkov, N. Glushkova, A. Ekhlakov, and E. Shapar, "An analytically based computer model for surface measurements in ultrasonic crack detection," *Wave Motion*, vol. 43, no. 6, pp. 458–473, 2006.

[30] V. Dorval, F. Jenson, G. Corneloup, and J. Moysan, "Accounting for structural noise and attenuation in the modeling of the ultrasonic testing of polycrystalline materials," in *AIP Conference Proceedings*, vol. 1211, 2010, pp. 1309–1316.

[31] J. Zhang, B. W. Drinkwater, and P. D. Wilcox, "Comparison of ultrasonic array imaging algorithms for nondestructive evaluation," *IEEE Trans. Ultrason., Ferroelectr., Freq. Control*, vol. 60, no. 8, pp. 1732–1745, 2013.

[32] A. Aubry and A. Derode, "Detection and imaging in a random medium: A matrix method to overcome multiple scattering and aberration," *J. Appl. Phys.*, vol. 106, p. 044903, 2009.

[33] S. Shahjahan, F. Rupin, A. Aubry, B. Chassignole, T. Fouquet, and A. Derode, "Comparison between experimental and 2-D numerical studies of multiple scattering in Inconel600® by means of array probes," *Ultrasonics*, vol. 54, no. 1, pp. 358–367, 2014.

[34] C. Dalitz, R. Pohle-Frohlich, and T. Michalk, "Point spread functions and deconvolution of ultrasonic images," *IEEE Trans. Ultrason., Ferroelectr., Freq. Control*, vol. 62, no. 3, pp. 531–544, 2015.

[35] L. Roquette, M. Simeoni, P. Hurley, and A. Besson, "On an analytical, spatially-varying, point-spread-function," in *IEEE International Ultrasonics Symposium*, 2017.

[36] N. Laroche, S. Bourguignon, E. Carcreff, J. Idier, and A. Duclos, "Fast inverse approach for the deconvolution of ultrasonic TFM images using a spatially varying PSF in NDT," in *IEEE International Ultrasonics Symposium*, 2019.

[37] L. Bai, A. Velichko, and B. W. Drinkwater, "Ultrasonic characterization of crack-like defects using scattering matrix similarity metrics," *IEEE Trans. Ultrason., Ferroelectr., Freq. Control*, vol. 62, no. 3, pp. 545–559, 2015.

[38] A. Velichko, "Quantification of the effect of multiple scattering on array imaging performance," *IEEE Trans. Ultrason., Ferroelectr., Freq. Control*, vol. 67, no. 1, pp. 92–105, 2020.

[39] E. Lopez Villaverde, S. Robert, and C. Prada, "Ultrasonic imaging of defects in coarse-grained steels with the decomposition of the time reversal operator," *J. Acoust. Soc. Am.*, vol. 140, no. 1, pp. 541–550, 2016.

[40] L. J. Cunningham, A. J. Mulholland, K. M. M. Tant, A. Gachagan, G. Harvey, and C. Bird, "The detection of flaws in austenitic welds using the decomposition of the time-reversal operator," *Proc. Royal Soc. A: Math., Phys. and Eng. Sc.*, vol. 472, no. 2188, 2016.

[41] J. P. McClure and R. Wong, "Multidimensional stationary phase approximation: boundary stationary point," *J. Comput. Appl. Math.*, vol. 30, no. 2, pp. 213–225, 1990.

Eduardo Lopez Villaverde received the Ph.D. degree in physics from Université de Paris, France. His Ph.D. research was carried out at the CEA-LIST, Gif-sur-Yvette, France, and was focused on ultrasonic imaging in complex materials using time reversal techniques.

From 2017 to 2018, he was a postdoctoral researcher at Institut Langevin, Paris, France, working on 3D ultrafast imaging for the extraction of ultrasonic features. From 2018, he has been a Research Associate at the Ultrasonics and Non-Destructive Testing research group, University of Bristol, U.K. His current research interests include ultrasonic array imaging, beamforming techniques, defect and material characterization.

Anthony J. Croxford was born in Hatfield, England, in 1979. He received an M.Eng. degree in mechanical engineering and a Ph.D. degree from the University of Bristol, Bristol, England, in 2005.

From 2005 to 2007, he was a Research Associate in the nondestructive testing research group at the University of Bristol, where he worked on the development of guided-wave structural health monitoring for permanently attached sensing systems. Since 2007, Dr. Croxford has been a Lecturer in the Department of Mechanical Engineering at the University of Bristol. His current research interests include structural health monitoring, nonlinear ultrasonic techniques, and ultrasonic array imaging.

Alexander Velichko was born in Krasnodar, Russia, in 1975. He received the M.Sc. degree in applied mathematics from Kuban State University, Krasnodar, in 1998, and the Ph.D. degree from Rostov State University, Rostov-on-Don, Russia, in 2002. His Ph.D. thesis was on the investigation of wave fields caused by internal vibration sources in layered elastic medium.

From 2005 to 2012, he was a Research Associate with Ultrasonics and Non-Destructive Testing Research Group, University of Bristol, Bristol, U.K. Since 2012, he has been with the Department of Mechanical Engineering, University of Bristol. His current research interests include mathematical modeling of propagation and scattering of elastic waves, guided wave inspection, ultrasonic imaging using arrays, defect characterization, and signal processing.